Energy 296 (2024) 131062

Contents lists available at ScienceDirect

Energy

journal homepage: www.elsevier.com/locate/energy

Experimental reconstruction of the local flow field in a Wells turbine using a three-dimensional pressure probe

Fabio Licheri *, Tiziano Ghisu, Francesco Cambuli, Pierpaolo Puddu

Department of Mechanical, Chemical and Materials Engineering, University of Cagliari, Via Marengo 2, 09123 Cagliari, Italy

ARTICLE INFO

Keywords:
Wells turbines
Experimental investigation
3D pressure probe
Non-stationary local measurements
Local turbine performance

ABSTRACT

Among the various solutions suggested for wave energy harvesting, the ones based on the oscillating water column (OWC) principle are considered as the most promising, due to their constructive simplicity and reliability. These systems convert sea wave energy into pneumatic energy in the form of a bi-directional airflow that can conveniently turned into mechanical energy by a Wells turbine. Since their introduction, Wells turbines have been studied extensively in order to characterize their performance. Most of the experimental studies have focused on global machine performance analyses, while the studies focusing on local performance analyses are limited. This work presents a detailed experimental investigation of a small-scale Wells turbine coupled to an OWC simulator. The turbine aerodynamic characteristic has been identified with global measurements, while a miniaturized aerodynamic probe has been used to evaluate local performance, by reconstructing the three-dimensional flow field upstream and downstream of the turbine during a complete regular wave period. Local analyses aid to explain global turbine performance, highlighting the main differences between inflow and outflow phases. Moreover, they allow to describe the variation in loading along the blade radius, and to evaluate the blade design law, which justifies the limited Wells turbine aerodynamic performance.

1. Introduction

Wave energy presents a large and widespread availability [1,2] and has the potential of attracting significant interest in light of the medium-term energy transition scenarios. Despite not being commonly used, also due to the relatively high levelized cost of energy (LCOE) associated [3], wave energy converters (WECs) employing different technologies have been studied extensively. Systems based on the oscillating water column (OWC) principle present higher reliability, simplicity of construction and are considered the most promising devices for large scale energy production [4], thanks to the absence of moving parts interacting with the sea water. These systems convert the potential energy of a water column moving inside an open chamber, partially submerged under the sea free surface, into the pneumatic energy of a column of air at the top of the chamber. The latter can be used to drive an air turbine to produce mechanical energy at its shaft. A simplified representation of the working principle of an OWC is shown in Fig. 1.

The airflow generated by an OWC system is periodic, time varying and alternate, meaning that its direction is inverted during system's operation. The alternate airflow requires a turbine capable to preserve its direction of rotation regardless of the flow direction, and this can be achieved by a Wells turbine [5]. The symmetric blades of this non-conventional turbine are staggered at 90 degrees with respect to the axis of rotation, as shown in Fig. 2, thus ensuring similar performance during outflow (air being pushed out of the chamber) and inflow phases (air flowing from the ambient into the chamber).

The Wells turbine's simplicity of construction and reliability have attracted a number of researchers who focused on the characterization of its performance [6,7], highlighting the main drawbacks associated to a limited torque at low incidence angles and a reduced operating range due to stall. The Wells turbine has been studied experimentally in early [8] and more recent studies [9,10], mainly with unidirectional setups, under fixed flow conditions. Only few experiments have reproduced the alternate flow typically present in an OWC system [11–14], while most of the experimental investigations available in the literature focus on overall performance characterization of laboratory-scale Wells turbines, measuring output torque and pressure drop across the rotor, together with the turbine rotational speed and flow rate. This approach is generally adopted to compare different rotor geometries [15] and operating conditions [10,16]. These data have been used for the validation of numerical results and then for optimization studies based on the improvement of local flow features, such as tip leakage [17–19] and separation [20,21]. Nevertheless, a detailed understanding of the local flow field is of significant importance to support more extensive validation of computation fluid dynamic (CFD) solvers, to increase the

* Corresponding author.
E-mail address: fabio.licheri@unica.it (F. Licheri).

https://doi.org/10.1016/j.energy.2024.131062
Received 25 September 2023; Received in revised form 8 March 2024; Accepted 19 March 2024
Available online 25 March 2024

Nomenclature

Acronyms

BDC	Bottom dead center
CFD	Computational fluid dynamics
CRV	Contra-rotating vortex
CV	Corner vortex
DIMCM	Department of Mechanical, Chemical and Materials Engineering
LCOE	Levelized cost of energy
LV	Leakage vortex
OWC	Oscillating water column
PTO	Power take-off
TDC	Top dead center
UPM	Uncertainty propagation method

Dimensional properties

α	Angle of the absolute flow
β	Angle of the relative flow
C	Absolute velocity
c	Blade chord
D	Turbine diameter
δ	Thickness
e	Specific energy
f	Frequency
l	Specific work
Ω	Angular rotational frequency
p	Pressure
Q	Volumetric flow rate
q	Dynamic pressure
r	Turbine radius
ρ	Air density
t	Time
$\mathcal{T}$	Torque
T_w	Piston period
U	Peripheral rotor speed
V	Velocity
W	Relative velocity
Z	Piston position

Non-dimensional properties

η	Efficiency
$H12$	Shape factor
K	Calibration coefficient
$K_{x,\phi}$	Turbine damping coefficient
ψ	Work coefficient
ν	Hub-to-tip ratio
p^*	Pressure drop coefficient
ϕ	Flow coefficient
$r^* = {(r-r_{hub})}/{(r_{tip}-r_{hub})}$	Non-dimensional turbine radius
$\mathcal{T}^*$	Torque coefficient
ξ_{EX}	Loss coefficient related to the exit kinetic energy
ξ_R	Loss coefficient related to the viscous losses
z	Number of blades
$Z^* = {(Z-Z_{BDC})}/{(Z_{TDC}-Z_{BDC})}$	Non-dimensional piston position

Subscripts and superscripts

1	Inlet
2	Outlet
f	Flow
hub	Turbine hub
is	Isentropic
$\overline{()}$	Mean/averaged value
r	Radial direction
ref	Reference value
θ	Tangential direction
tip	Turbine tip
ts	Total-to-static
z	Axial direction

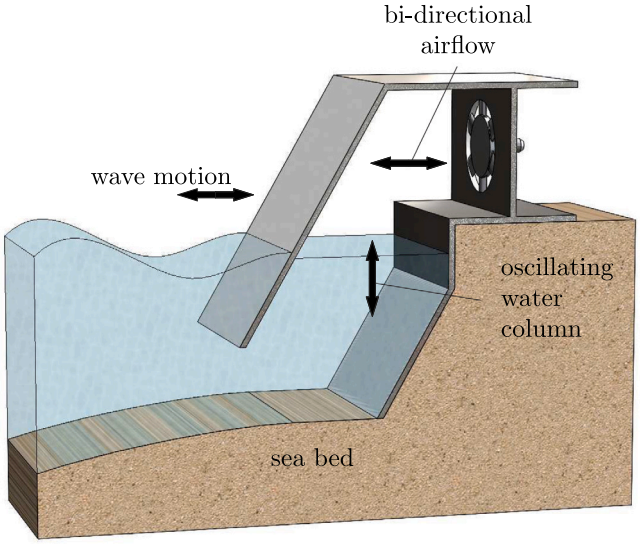

Fig. 1. OWC working principle.

confidence in the analysis and optimization of these complex local flow features.

Most of the local flow investigations have been conducted assuming the flow to be two-dimensional, i.e. neglecting the radial velocity component. Alves et al. [22] have investigated the (assumed) 2D flow inside a biplane Wells rotor with and without intermediate guide vanes, in order to observe the local flow modification due to the presence of a row of stator blades; Morais et al. [23] have extended this work, testing and comparing different biplane Wells rotors by measuring the local flow-field assumed as 2D; Licheri et al. [24] have performed 2D measurements for an isolated monoplane Wells turbine coupled to an OWC simulator, presenting local performance for a wide range of operating conditions only during the inflow phase. Local 3D flow investigations can be found in Puddu et al. [25], only at the blade midspan, for a Wells turbine under bi-directional flow, while Licheri et al. [26] reconstructed the local flow field downstream of a Wells rotor within a blade pitch, for a fixed flow condition, using a hot-wire anemometer. Table 1 summarizes the local flow analyses on Wells turbines available in the literature, highlighting the types of rig used and of flow investigations.

To the authors' knowledge, this paper investigates for the first time the three-dimensional flow field upstream and downstream of a Wells turbine rotor operating under a regular periodic bi-directional airflow, at different radial positions. A four-holes aerodynamic probe, designed and built for the purpose, has been used for this investigation, aiming to

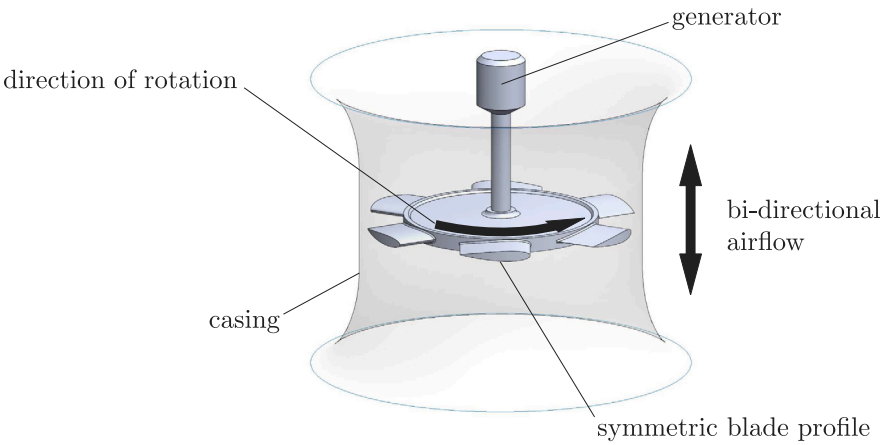

Fig. 2. Wells turbine working principle.

Table 1
Contribution to local flow measurements in Wells turbines.

Reference	Setup/Flow conditions	Flow investigation	Notes
Gato, Falcão [8]	Unidirectional/steady state	Mean 2D flow along the blade span	Theoretical vs. experimental prediction of rotors with different solidities
Curran, Gato [27]	Unidirectional/steady state	Mean absolute flow angle at the outlet	Test of different designs of mono- and multi-plane Wells turbines
Gato, Webster [28]	Unidirectional/steady state	Mean absolute flow angle at the outlet	Comparison of swept and unswept blades for different rotor solidities and pitch angles
Paderi, Puddu [25]	OWC simulator/non-stationary	Mean 3D flow at midspan	Performance of a high solidity monoplane Wells turbine
Puddu et al. [12]	OWC simulator/non-stationary	2D flow in a blade pitch at midspan	Instantaneous performance of a high solidity monoplane Wells turbine
Licheri et al. [24,29]	OWC simulator/non-stationary	Mean 2D flow along the blade span	Local performance of a high solidity Wells turbine, relative contribution of losses
Alves et al. [22], Morais et al. [23]	Unidirectional/steady state	Mean 2D flow along the blade span	Effects of intermediate guide vanes between a biplane Wells turbine
Licheri et al. [26]	OWC simulator/unsteady	3D flow in a blade pitch along the blade span	Local flow structures in a blade pitch and their extension for a fixed flow rate condition

define the time-dependent local performance of the Wells rotor. Based on the flow reconstruction, differences in performance between inflow and outflow phases, already observed in previous works, have been explained and related to the differences in the incoming flow. On the other hand, the effect of the radial component, usually neglected in experimental Wells turbine measurements, has been evaluated, as it is expected to be relevant for the particular rotor tested due to the reduced blade height. Moreover, the flow reconstruction has been used to recover the blade design law, as Wells turbines are often designed with a constant blade chord along the span. The implication on the expected rotor performance of this simple design has been investigated for the very first time. A newly built Wells turbine prototype has been adopted for the present analysis, with a value of the rotor solidity close to the ones found in literature [13,27,30,31]. In addition, the OWC simulator in the Department of Mechanical, Chemical and Materials Engineering (DIMCM) at the University of Cagliari has recently been upgraded to allow a simpler and more rapid installation of measuring instruments. It features a straight (axial) inflow duct, similar to the ones conventionally used in real installations, which replaces the curved duct used in previous analyses [12,24,25,29].

This paper is organized as follows: Section 2 introduces the experimental rig and the instrumentation used for the present analysis, providing a detailed description of measured signals, probe calibration and sensors' estimated uncertainties. Traditional performance parameters are defined in Section 3, together with two additional non-dimensional parameters useful to define local rotor performance. Results for the inlet and outlet flow, as well as both overall and local rotor performance, are described in Section 4. Section 5 summarizes the main findings of this analysis and draws conclusions.

2. Experimental setup and instrumentation

The OWC simulator housed in the DIMCM at the University of Cagliari has recently been upgraded by modifying the measuring and outlet sections at the ambient side, previously characterized by a curved configuration with a radial exit section [12,24,25,29]. A sketch of the modified setup is shown in Fig. 3, where the straight (axial) configuration of the exit duct at the top of the rig is evident. The newly built ambient-side section has been introduced to ensure a better symmetry between inflow and outflow phases, which was previously not possible due to the radial gradients caused by the curved duct. The new setup will allow to isolate the different contributions given by the presence of the chamber during inflow and outflow, while its more common geometry will provide results of general validity for the aerodynamic behavior of the Wells turbine.

The OWC simulator is composed of a cylindrical steel chamber where a piston, driven by a hydraulic unit, is used to mimic the

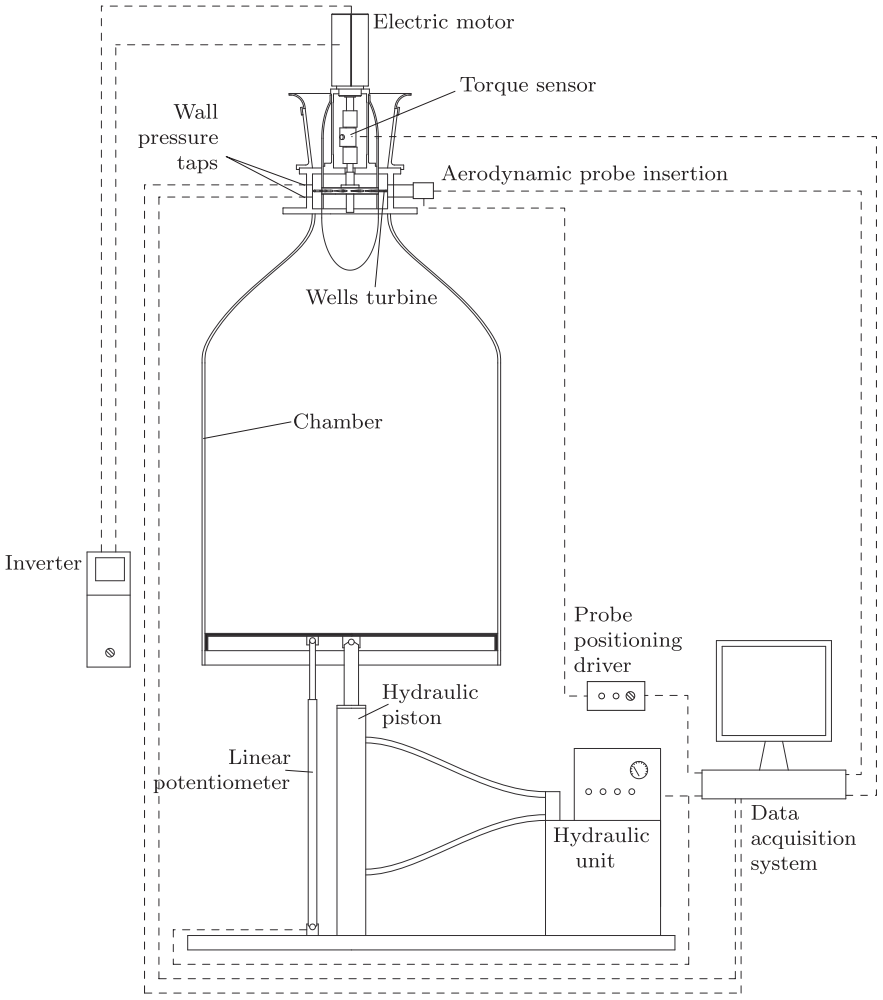

Fig. 3. Experimental setup scheme.

periodic motion of a water column inside an OWC. Different wave states can be reproduced with this experimental setup by changing the amplitude and frequency of the periodic motion of the piston, ensuring a maximum flow speed of about 20 m/s at the inlet of the rotor. The piston displacement set for the present analysis, a regular sinusoidal motion, is represented in Fig. 4, together with the flow coefficient, which is obtained by non-dimensionalizing the axial component of the flow speed upstream of the rotor (C_z) with the turbine's peripheral velocity at the tip (U_{tip}). Refer to Eq. (5) for a definition of the turbine non-dimensional performance parameters.

Every piston period can be divided in two semi-periods. During the first one, the piston moves from the top dead center (TDC) to the bottom dead center (BDC) and the air flows into the turbine from the ambient: we refer to this semi-period as the inflow phase. Then, when it returns to the TDC, the piston pushes air from the OWC chamber through the turbine: we refer to this semi-period as the outflow phase. The axial component of the velocity C_z (and therefore the flow coefficient ϕ) is assumed positive during outflow, and negative during inflow. Each one of these semi-periods can be further subdivided into an acceleration and a deceleration phase, depending on whether the absolute value of the flow coefficient is increasing or decreasing. The different phases of a piston period and their nomenclature are highlighted in Fig. 4.

A linear wire potentiometer is employed to measure the piston displacement and for the feedback control of the hydraulic unit. Above the chamber, a Wells turbine, which drives an electric motor controlled by an inverter with encoder feedback, is installed. The main geometric parameters of the turbine are summarized in Table 2.

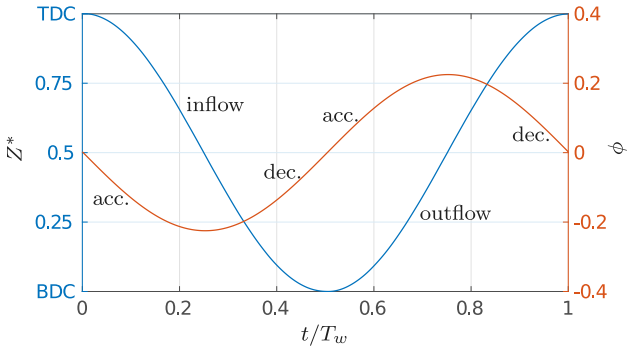

Fig. 4. Non-dimensional piston motion and flow coefficient variation obtained in the experiment.

A shaft-to-shaft torque sensor is placed between the turbine and the electric motor, and it also allows to measure the turbine rotational speed with a built-in optical encoder. The measuring section, shown in Fig. 5(a), is equipped with wall pressure taps placed on both sides of the rotor at a distance of ±7.5 mm from the blade chord. Three taps have been placed at each side of the rotor (equally spaced around the annulus) and connected with two transducers, one per side, properly selected with respect to expected pressure values (see Table 3). Aerodynamic probes can also be inserted in this section and a positioning driver allows them to be moved along the machine radial direction and

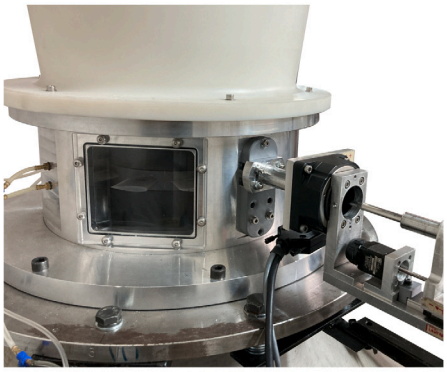

(a) Picture of the measuring section.

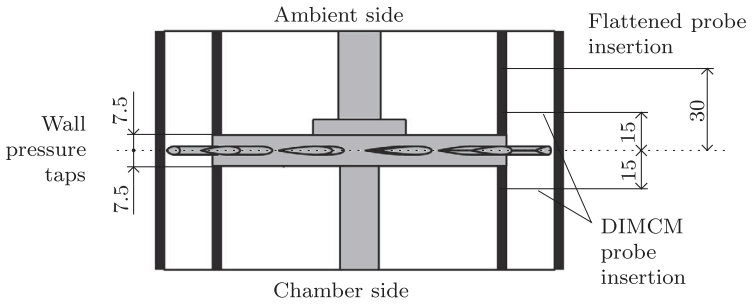

(b) Schematic view of the measurement positions (in mm).

Fig. 5. Location of the measurement stations near the turbine.

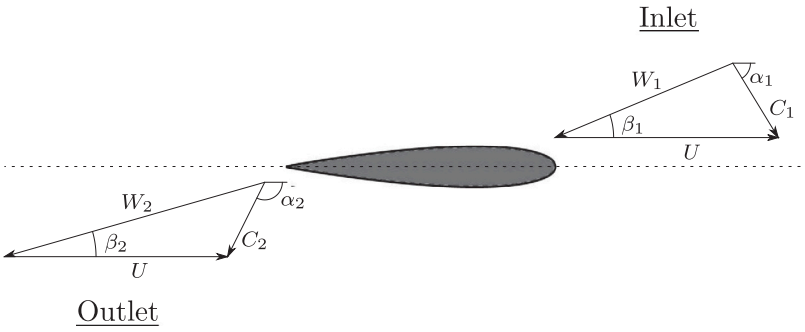

Fig. 6. Velocity triangles upstream and downstream the Wells rotor.

Table 2
Geometric parameters of the tested Wells turbine.

Rotor tip diameter, D_{tip}	250 mm
Rotor hub diameter, D_{hub}	190 mm
Tip clearance	1 mm
Chord length, c	36 mm
Number of blades, z	12
Airfoil profile	NACA 0015
Solidity	0.625
Sweep ratio	0.5 (18/36)
Hub-to-tip ratio, ν	0.76

to be rotated around their axis. This system also allows to adjust the probe's distance from the blade chord, in the machine axial direction. A detailed scheme of the measurement positions is shown in Fig. 5(b).

The volumetric flow rate cannot be measured with standardized flowmeters, due to the configuration of the setup, but it can be calculated based on the piston position (recorded with the linear potentiometer), taking into account the time delay between the piston motion and the corresponding flow speed at the rotor inlet, due to the presence of the chamber volume [25]. Expected uncertainties for the global measurements (torque, wall static pressures and piston position) are listed in Table 3, together with the most relevant properties of each measuring device in use.

2.1. Aerodynamic probe

The local three-dimensional flow field properties both upstream and downstream of the turbine have been reconstructed using a 4-holes aerodynamic probe, similar to a wedge probe [32,33] and built for the purpose. Representative velocity vectors at the inlet and outlet of the Wells rotor are shown in Fig. 6. These angle definitions have been used in the following flow field reconstruction.

A schematic of the DIMCM probe is presented in Fig. 7(a), while the picture in Fig. 7(b) shows the insertion near the Wells turbine rotor, at a distance of 15 mm from the blade chord as set during the tests.

The custom-made probe has been designed and built for this specific setup: it has a maximum head size of about 2.5 mm in the radial direction, thus allowing a fine scan resolution along the blade span while minimizing the distortion of the flow field. This is particularly important considering the reduced blade height. The probe's head is placed on a stem with a diameter of 3 mm, as shown in Fig. 7(b).

The aerodynamic probe has been used in "non-nulling" mode within its angular calibration range, in order to determine the flow angles and total and static pressures. Probe orientations have been selected according to the expected flow directions, both at the inlet and at the outlet of the turbine, by rotating the stem of the probe around its axis. The angular calibration has been conducted in a subsonic wind tunnel, by relating the pressure values measured by the probe holes indicated in Fig. 7(a) with the true values, i.e. the total pressure p_t and the static pressure p of the flow field in the wind tunnel, and to the flow angles. The following non-dimensional coefficients have been used to describe the angular calibration of the probe, adopting definitions similar to the ones used for other multi-hole aerodynamic probes in the literature [32]:

$$K_Y = \frac{p_{left} - p_{right}}{q_{probe}} \tag{1}$$

$$K_P = \frac{p_{up} - p_{down}}{q_{probe}} \tag{2}$$

$$K_T = \frac{p_t - p_{front}}{p_t - p} \tag{3}$$

$$K_S = \frac{p - p_s}{p_t - p} \tag{4}$$

where K_Y, K_P, K_T and K_S represent the yaw coefficient, the pitch coefficient and the total and static pressure coefficients, respectively;

Table 3
Properties of the instruments used to characterize global performance (FSS stands for Full Scale Span).

Measured variable	Sensor	Range	Accuracy	Sensitivity
Wall static pressure at rig ambient side	Sensor technics BSDX series	±1 kPa	±1 %FSS	2.0 V/kPa
Wall static pressure at rig piston side	Sensor technics BSDX series	±1 PSI	±0.5 %FSS	2.0 V/PSI
Output torque	ETH messtechnik type DRFL-I	±2 Nm	±0.1 %FSS	2.5 V/Nm
Piston position	MAFEurope - DWT series	1.5 m	0.5 %FSS	3.3 V/m
Turbine rotational speed	(built-in in the torque sensor)	10 000 rpm	±1/60 rpm	–

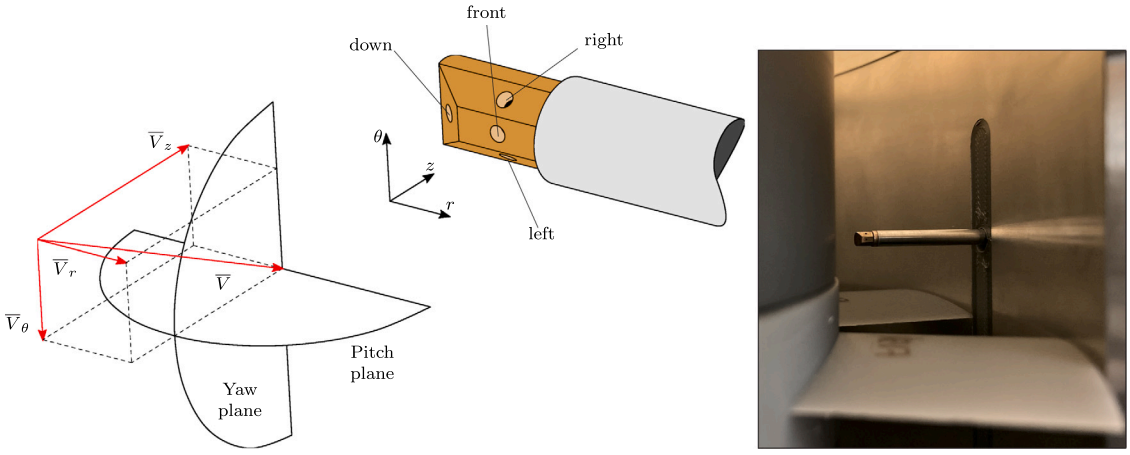

(a) Schematic view of the DIMCM probe.

(b) Probe insertion in the measuring section.

Fig. 7. DIMCM probe schematic view and its positioning near the turbine.

p_{up} is calculated by averaging left and right pressures, i.e. $p_{up} = (p_{left} + p_{right})/2$; p_s represents the "static pressure" of the probe, calculated as the mean of the directional pressure values $(p_{down} + p_{left} + p_{right})/3$ and q_{probe} represents the "dynamic pressure" of the probe, $p_{front} - p_s$. The schematic representation in Fig. 7(a) shows the probe's taps and their names. The directional taps, i.e. down, left and right taps, and the total pressure tap, named as front, are clearly identifiable.

The pitch and yaw angles are measured in the pitch and yaw planes, respectively, as sketched in Fig. 7(a). According to Eqs. (1) and (2), the pitch is considered positive when the flow encounters the probe from the "up" direction, while the yaw angle is positive when the flow comes from the left tap's side. Contour maps of the calibration coefficients defined in Eqs. (1)–(4) are shown in Fig. 8 as a function of the flow angles, as evaluated during the calibration process.

The lack of symmetry for the probe's response in the pitch plane is clearly visible (see Fig. 8(b)) and is due to both the asymmetry of the probe's head in the pitch plane and to the presence of the stem. The range of reliable use should not exceed the calibration ranges, i.e. ±30 degrees. Probe symmetry in the yaw plane is clearly observed, while a good directional sensitivity of the probe is shown in Fig. 8, with respect both to the yaw and to the pitch angle. Nevertheless, the errors on total and static pressure measurements, represented by K_S and K_T, are, as expected, dependent on both flow angles and tend to become larger with the misalignment between the probe and the flow direction.

Differential signals, i.e. $p_{left} - p_{right}$ and $p_{front} - p_{down}$, have been measured in order to minimize the uncertainty in the determination of the flow angles, as demonstrated in [34]. In addition, single gauge pressures for front and left taps have been also acquired, in order to evaluate all pressure terms. Four differential pressure transducers have been used to collect all these signals, as summarized in Table 4.

Measurements' uncertainties have been evaluated with the classic uncertainty propagation method (UPM) [35]. The uncertainties on calibration coefficients K_Y, K_P, K_T and K_S have been estimated from the calibration process, as done in [34]. The estimated maximum uncertainties in both flow angles is around ±0.5 degrees. Total and static pressures have shown a maximum uncertainty of about ±15 and ±20 Pa, respectively. Therefore, the maximum flow speed uncertainty based on the UPM results in a value of ±0.5 m/s.

The DIMCM probe has been used to investigate the inlet and outlet flows, both during inflow and outflow, by taking pressure measurements at ambient and piston sides. The blade span has been scanned at 18 radial positions, not equally spaced: smaller steps of less than 1 mm have been taken near the walls where larger pressure gradients were expected. Local measurements have been performed under time-varying flow conditions, as done for global measurements. All the settings used in the experiments are listed in Table 5.

The turbine rotational frequency has been selected to obtain a maximum flow coefficient of about 0.22, as listed in Table 5, at the limit of the stall-free operating range. The inverter's PID controller provides an almost constant turbine rotational speed, by means of a feedback encoder signal.

The acquisition time at each probe position has been set to acquire signals for at least 5 piston periods with a sampling rate of 1 kHz. An average distribution of the acquired signals has been obtained with a phase locked averaging process based on piston movement. This allowed to obtain signals at a reduced number of points (250 points per period), as shown in Fig. 9 for the non-dimensional global measured quantities, where the grey lines represent 5 overlapped piston cycles measurements.

No significant differences can be observed for position and wall-pressure measurements between different periods, and, as a consequence, the phase averaged results appear close to the original measures. Larger differences can be observed for output torque and turbine rotational frequency, as expected due to the nature of these signals and the high sensitivity of the torque sensor which records both these quantities. Nevertheless, signals bandwidths are narrow and the data reduction process does not distort the original measurements. Uncertainties, represented as black vertical lines, are larger for torque and

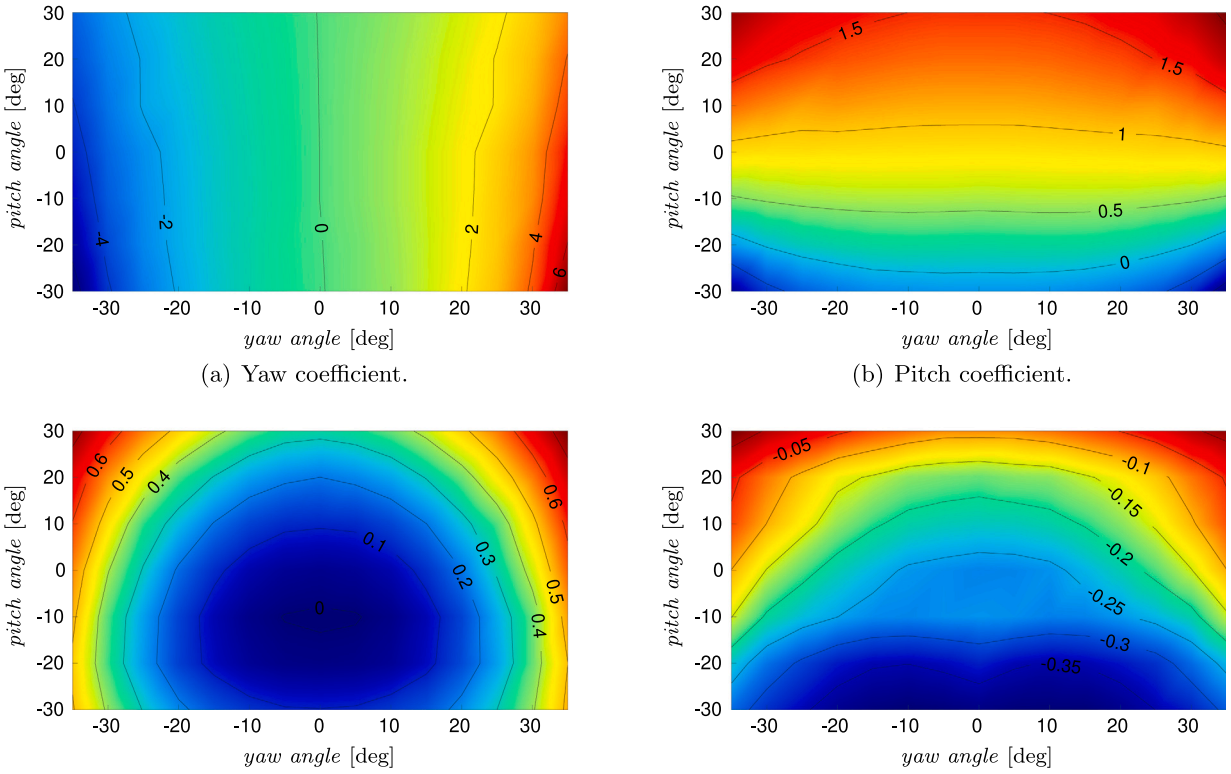

(a) Yaw coefficient. (b) Pitch coefficient.

(c) Total pressure coefficient. (d) Static pressure coefficient.

Fig. 8. Non-dimensional calibration coefficients for the DIMCM probe.

Table 4
Pressure transducers used with the DIMCM probe (FSS stands for Full Scale Span).

Measured variable	Sensor	Range	Accuracy	Sensitivity
p_{front}	Sensor technics BSDX series	±2.5 kPa	±1 %FSS	0.8 V/kPa
$p_{left} - p_{right}$	Sensor technics BSDX series	±2.5 kPa	±1 %FSS	0.8 V/kPa
$p_{front} - p_{down}$	Sensor technics BSDX series	±2.5 kPa	±1 %FSS	0.8 V/kPa
p_{left}	Sensor technics BSDX series	±2.5 kPa	±1 %FSS	0.8 V/kPa

Table 5
Experimental settings.

Turbine rotational frequency, f	60 Hz
Piston stroke amplitude	≈850 mm
Piston period, T_w	9 s
Maximum flow coefficient, ϕ	0.22
Reynolds' number at exit conditions and based on blade chord	1.35×10^5

rotational frequency, as expected, while they are significantly smaller for position and wall pressure measurements.

3. Turbine performance

In order to characterize the performance of a Wells turbine, the following non-dimensional parameters are typically adopted [8]: the flow coefficient ϕ, the torque coefficient $\mathcal{T}^*$ and the pressure coefficient p^*:

$$\phi = \frac{C_z}{\Omega r_{tip}} \qquad \mathcal{T}^* = \frac{\mathcal{T}}{\rho \Omega^2 r_{tip}^5} \qquad p^* = \frac{\Delta p}{\rho \Omega^2 r_{tip}^2} \tag{5}$$

where C_z is the (spatially averaged) axial flow velocity at the turbine inlet, calculated based on the piston speed, and accounting for the phase difference due to the capacitive behavior of the OWC [36]. The static pressure drop Δp is the pressure difference across the turbine obtained from the wall pressure measurements at either sides of the machine [8]. Performance parameters, as defined in Eq. (5), can be estimated based on global measurements, i.e. the output torque, the rotational speed of the turbine, the wall static pressures and the piston velocity, and are useful to give an overall characterization of the turbine. Starting from these global measurements, the turbine efficiency can readily be defined as in [6,8]:

$$\eta = \frac{\mathcal{T}\Omega}{\Delta p Q} = \frac{\mathcal{T}^*}{p^* \phi} \frac{1}{\pi(1-\nu^2)} \tag{6}$$

where ν is the turbine's hub-to-tip ratio. In the present work, $\mathcal{T}$ refers to the aerodynamic torque, obtained by clearing the torque measured at the turbine shaft from windage and friction losses and from the rotor inertial torque. Thus, the associated efficiency calculated with Eq. (6) represents an aerodynamic efficiency, as explained in [21]. The UPM has been applied to the calculated non-dimensional performance, starting from the measurements' uncertainties in Fig. 9. Thus, a maximum relative uncertainty of ±8.8% has been calculated for T^*, a value of ±1.1% has been estimated for p^*, a value of ±1.6% for ϕ, while a slightly larger value, equal to ±9.0%, has been obtained for the efficiency η.

A more appropriate efficiency formulation should consider that in a Wells turbine the exhaust kinetic energy is not recovered, as pointed

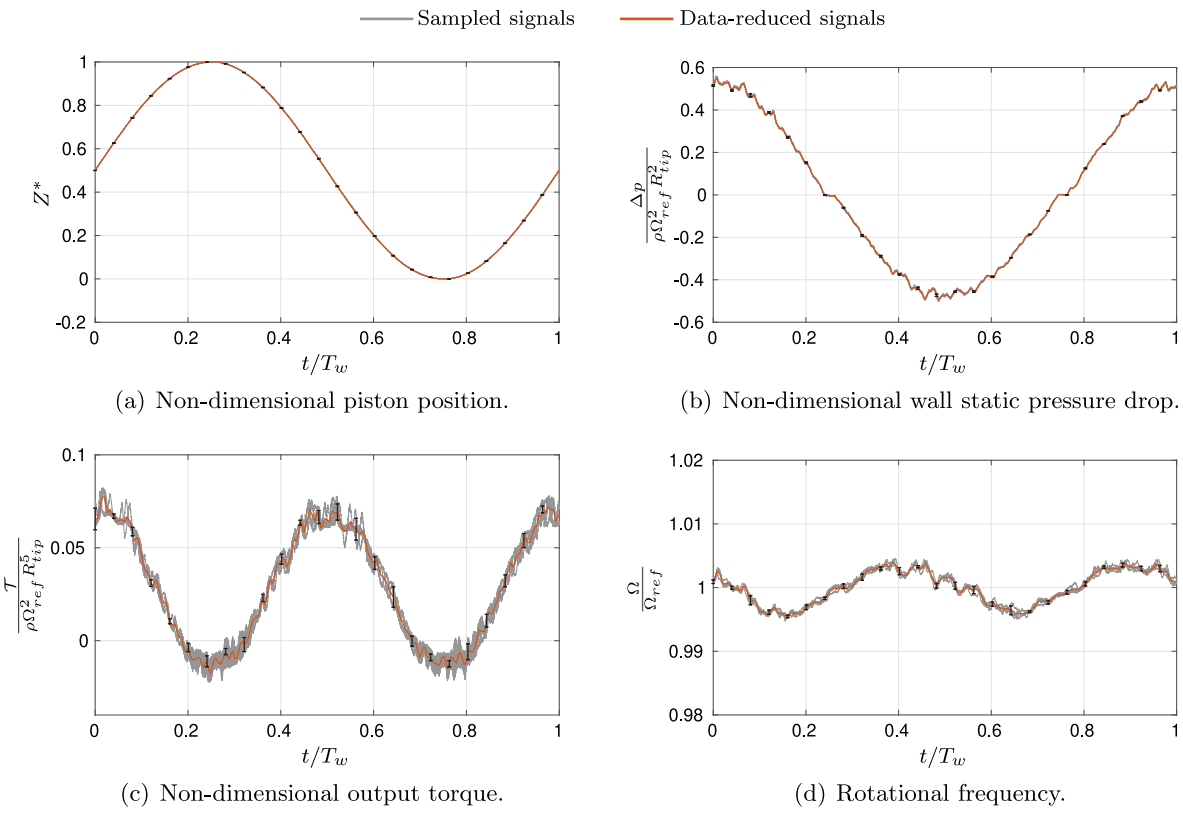

(a) Non-dimensional piston position.

(b) Non-dimensional wall static pressure drop.

(c) Non-dimensional output torque.

(d) Rotational frequency.

Fig. 9. Measured quantities in successive tests and data-reduction result.

out in [7,21,37]. Therefore, the total-to-static efficiency can be used for this purpose:

$$\eta_{ts} = \frac{\mathcal{T}\,\Omega}{(p_{t1} - p_2)Q} \tag{7}$$

The latter can be evaluated based on the above global measurements only for the inflow phase, where the total pressure at the turbine's inlet can be reasonably assumed equal to the atmospheric pressure, if inlet duct pressure losses are neglected [29]. The same approximation cannot be taken for the outflow phase as the total pressure at the chamber side needs to be directly measured, given the presence of a swirling flow. As an alternative, it could be approximated using local measures, i.e. combining static pressure and flow velocity obtained from the probe.

Local performance can be described by introducing the work coefficient ψ, see Eq. (8), which represents the specific work $l(r)$, exchanged between fluid and machine at a specific radial position r, non-dimensionalized with respect to the tip peripheral velocity.

$$\psi(r) = \frac{l(r)}{U_{tip}^2} = \frac{\left[U(C_{1\theta} - C_{2\theta})\right]_r}{U_{tip}^2} \tag{8}$$

In a previous work [29], the authors have shown that the total-to-static efficiency can be expressed as

$$\eta_{ts} = 1 - \xi_R - \xi_{EX} \tag{9}$$

where ξ_R and ξ_{EX} are the loss coefficients related to viscous losses (the rotor losses) and exit kinetic energy, respectively. This formulation of η_{ts} can be applied along the blade span, using the flow properties reconstructed from the probe measurements.

Relative uncertainties in both the work coefficient ψ and the total-to-static efficiency η_{ts} have been evaluated, considering the probe's maximum errors after the flow reconstruction process. A value of $\pm 3.6\%$ has been found for ψ while a value of $\pm 7.1\%$ has been calculated for η_{ts}.

A detailed analysis of the relative contributions due to the two loss mechanisms has been presented, for a different Wells turbine geometry, in [29]. In the present analysis, these two contributions will be evaluated for the inflow and outflow phases, in order to understand their relative impact on the total-to-static efficiency calculation. A detailed derivation of the two coefficients can be found in [29].

4. Results

4.1. Turbine overall characteristic

The turbine performance is reported in Fig. 10, in terms of the non-dimensional parameters and the global efficiency defined in Eqs. (5) and (6).

Performance is shown for a wide operating range in the stall-free region, with a maximum value of the flow coefficient $\phi \approx 0.22$. The turbine aerodynamic efficiency shows an almost constant value in a relatively wide range of operating conditions, with the exception of the proximity to the piston inversion and near the maximum value of flow coefficient, where a slight drop is present. The pressure drop coefficient shows a linear trend with respect to the flow coefficient ϕ, away from the inversion, and the slope of this curve, equal to 2.59, represents the damping coefficient of the turbine, $K_{x,\phi}$, which is a fixed property of the tested turbine. The values of the performance parameters obtained from measurements both during acceleration and deceleration are represented in Fig. 10, as blue dots, without distinction. No significant differences are present, as expected given the low non-dimensional frequency $(\pi f c)/U$ of about 3.9×10^{-4} [38]. The performance of the machine can therefore be represented as a single curve for each of the parameters, function of the non-dimensional flow coefficient ϕ. The interpolating curves obtained are shown as dashed black lines in Fig. 10.

Performance parameters in Fig. 10(a) and (c) present different values between inflow (negative values of ϕ) and outflow (positive

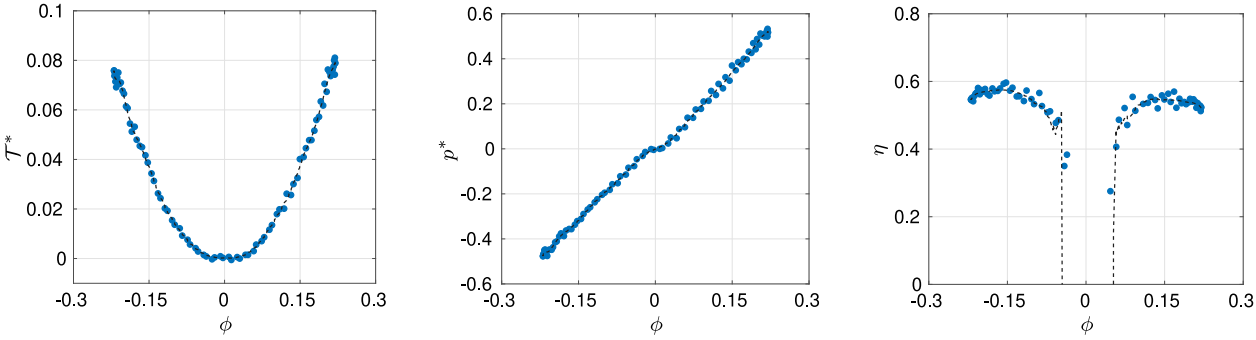

(a) Torque coefficient. (b) Pressure drop coefficient. (c) Aerodynamic efficiency.

Fig. 10. Non-dimensional characteristics of the Wells turbine.

values of ϕ) phases, as often observed for Wells turbine coupled to OWC systems [12,25]. Local measurements, reported in Sections 4.2 and 4.3, will help to explain this aspect of the turbine behavior.

The mean aerodynamic efficiency in a cycle of the turbine has been evaluated as follows:

$$\overline{\eta} = \frac{\int_{T_w} \mathcal{T}\,\Omega\,\mathrm{d}t}{\int_{T_w} \Delta p\,Q\,\mathrm{d}t} \tag{10}$$

and a value of 53.0% has been obtained for $\overline{\eta}$ in the selected operating range ($-0.22 \le \phi \le 0.22$).

4.2. Inlet flow

A preliminary investigation of the inlet boundary layer has been conducted by measuring the total pressure variation along the blade span with a very small flattened probe (nose radial dimension equal to 0.35 mm). Measures have been taken only at the ambient side, i.e. during the inflow phase, the only condition when the flow is truly axial, as it will be shown in detail later in this Section. The probe has been placed 30 mm (about a chord) upstream of the rotor, as shown in Fig. 5, and the total pressure has been measured at 32 radial positions, refined in the near-walls regions with a minimum radial step size of 0.35 mm, a value similar to the size of the probe's nose. The static pressure measured from the wall pressure taps has been used to calculate the velocity profile. While total and static pressure measurements were taken at slightly different axial positions, the impact of this offset is expected to be small, due to the constant cross-section of the duct. Fig. 11 shows the absolute velocity C non-dimensionalized with respect to the mean velocity C_{ref} (outside the boundary layer) as a function of the non-dimensional radial position r^*.

The velocity profile presents thin boundary layers, both near tip and hub walls, with a maximum thickness of less than 14% of the blade span. The boundary layer shape in Fig. 11 is representative of a turbulent flow. The clean flow appears very uniform and well defined, thus confirming that the newly built inlet duct at the ambient-side does not introduce any flow distortion to the turbine. 12 measuring points fall within the boundary layer, a number that is deemed adequate to estimate some common integral boundary layer measures.

A summary of these integral boundary layer parameters, calculated assuming flow incompressibility as proposed by [39] and justified by the low Mach number values, is reported in Table 6, both for the tip and hub boundary layers. These parameters provide a detailed description of the inlet boundary layer of the tested turbine, and they represent important information to perform numerical simulations with the correct boundary conditions.

The velocity components and flow angles at the turbine's inlet, reconstructed with the DIMCM probe, are shown in Fig. 12, as a function

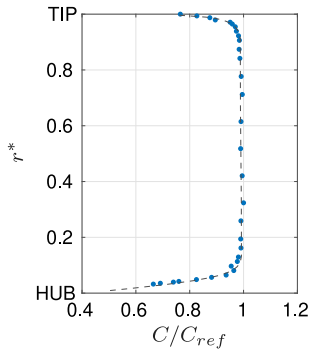

Fig. 11. Inlet velocity distribution during the inflow phase, at the ambient side, for $\phi = 0.195$.

Table 6
Integral boundary layer parameters.

	Hub wall	Tip wall
Thickness, δ_{99}	4.1 mm	2.7 mm
Displacement thickness, δ_1	0.23 mm	0.17 mm
Momentum thickness, δ_2	0.19 mm	0.16 mm
Shape factor, H_{12}	1.2	1.1

of the non-dimensional piston period and of the non-dimensional radial position, both during inflow and outflow.

The inlet flow presents an almost uniform distribution along the blade span with the exception of the proximity to the hub and tip regions. The wall effect is more evident in the tip region during the outflow phase where the inlet flow shows three-dimensional characteristics (high radial velocity component in Fig. 12(b)). Both in the tip and hub regions, the radial velocity component shows positive values which mean that flow is moving from the hub to the tip of the blade. Near the hub, this can be related to the high rotor solidity which exerts a blockage on the flow. In the tip region, the presence of the tip gap draws the flow to higher radii. A tangential velocity component is present during the outflow phase due to the rotation exerted on the air contained in the chamber during the previous phase, and its value increases along the span, from the hub to the tip. As a consequence, the absolute flow angle α_1 slightly varies from hub to tip, as shown in Fig. 12(d). Also the incidence angle β_1 shows a linear variation along the blade span, decreasing when moving from the hub to the tip during both phases, and this can be attributed to the variation of the peripheral velocity with the rotor radius. Flow angles have been reported also in Fig. 13: Fig. 13(a) present their variation as a function of time during a piston period, at midspan, while Fig. 13(b) shows the variation of the flow angles along the blade span, for a fixed value of the flow coefficient ($\phi = 0.22$), and hence for a given time during a piston period.

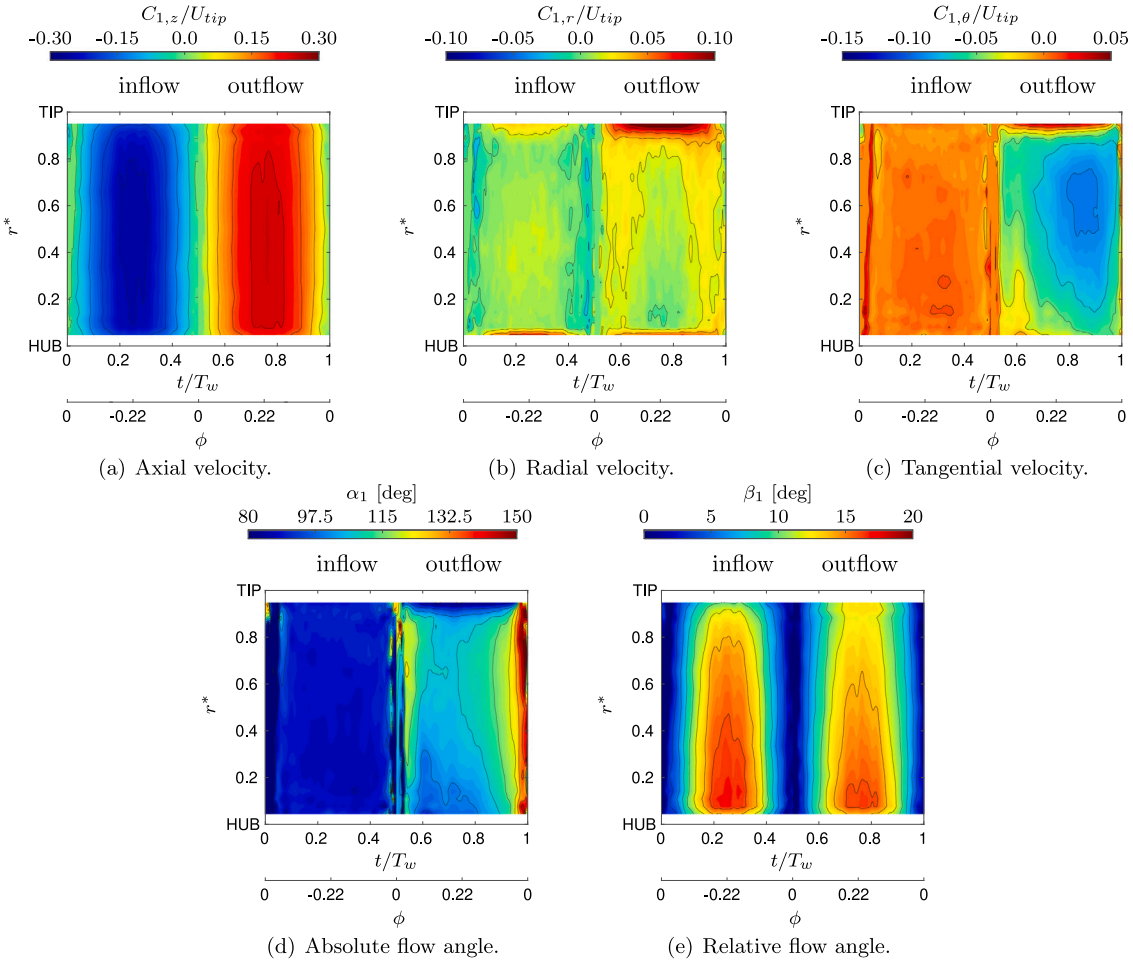

(a) Axial velocity. (b) Radial velocity. (c) Tangential velocity.

(d) Absolute flow angle. (e) Relative flow angle.

Fig. 12. Maps of velocity components and flow angles at the turbine inlet for a complete piston period.

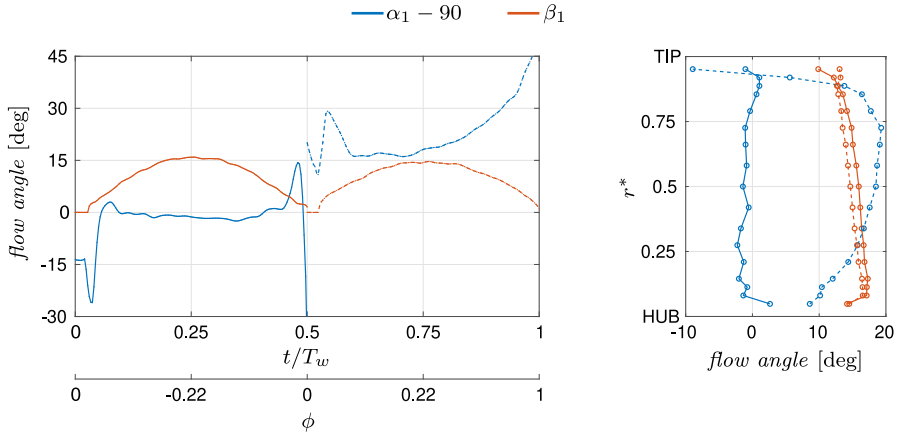

(a) Flow angles at blade midspan. (b) Flow angles for $\phi = 0.22$.

Fig. 13. Inlet flow angles distributions during the inflow (solid line) and outflow phase (dashed line).

These representations highlight the differences between the turbine inlet flow during inflow and outflow phases, caused by the presence of the swirling flow during outflow. The swirl velocity component is not constant during the piston period, hence it is not constant with the operating condition established by the piston motion, as previously pointed out in [12], and it grows along the blade span. The presence of this swirl velocity during outflow reduces the maximum value of β_1, compared to the inflow phase. This is at the origin of the difference in performance between the two phases shown in Fig. 10. After about $t/T_w = 0.75$, $C_{1,\theta}$ is almost constant and the reduction in the axial component results in an increased α_1, noticeable in Fig. 13(a). The aerodynamic load on the rotor and also the stall point directly depend on the incidence angle. The effect of this difference in incidence between the two phases on the turbine performance will be clarified in Section 4.4.

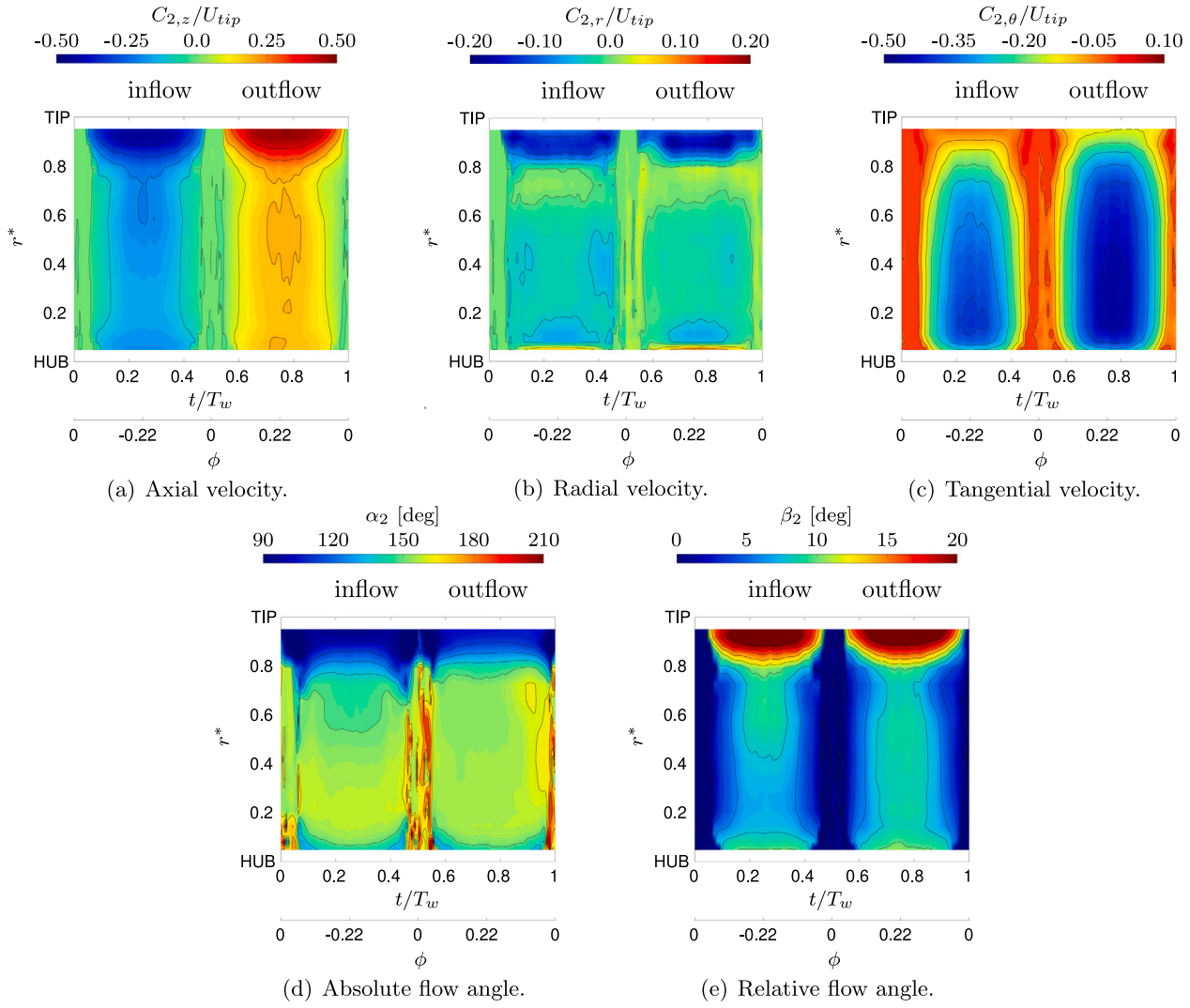

Fig. 14. Maps of velocity components and flow angles at the turbine outlet for a complete piston period.

4.3. Outlet flow

Velocity and flow angle distributions along the blade span, measured at turbine's outlet, are reported in Fig. 14, during both inflow and outflow phases. As expected, they show the same trends and very small differences can be observed for the axial and radial velocity distributions while more evident are the differences in the tangential velocity distributions (see Fig. 14(c)). At the turbine outlet, a small negative radial velocity component is detected for both the flow phases and intense three-dimensional effects are present near hub and tip regions. The larger radial gradients near the tip for both the axial and radial velocity components can be associated to the leakage flow, which extends to a relevant portion of the blade height, i.e. for about 20% of the blade span. In particular, the higher values of the axial component $C_{2,z}$ in this region suggest the presence of a jet flow, which has been observed also with more detailed flow investigations in [26], although under stationary operating conditions. Negative values of the radial component at the tip suggest that the leakage flow, at this axial position, is moving to lower radii, coherently to what observed from numerical simulations on similar Wells turbines [18,19]. As a consequence of the leakage flow, the blade load is strongly reduced in the tip region, as highlighted in the trends of the tangential velocity component $C_{2,\theta}$ and of both the absolute and relative flow angles, i.e. α_2 and β_2.

Small positive values of the radial velocity component are present near the hub, while negative values appear above. This distribution is compatible with the presence of a small confined corner vortex near the hub, while the above flow appears to be drawn towards the hub due to the specific distribution of work (see Fig. 17) and the presence of a low energy flow near the hub.

The tangential velocity component during inflow shows a lower intensity than in the outflow phase, and this can be considered as a consequence of the different characteristics of the flow at the rotor inlet, as highlighted in Section 4.2. The absolute flow angle (α_2) distribution is almost constant along the blade height and only small differences between the two phases occur, mainly at large radial positions (see Fig. 14(d)) due to the presence of a more pronounced inlet swirl. Outlet flow angles have been reported also in Fig. 15: Fig. 15(a) presents their variation as a function of time during a piston period, at midspan, while Fig. 15(b) shows the variation of flow angles along the blade span, for a fixed value of flow coefficient ($\phi = 0.22$), and hence for a given time during a piston period.

The trend of α_2 suggests that the different operating condition or the incidence angle β_1 have a limited effect on the absolute flow angle at the outlet (Fig. 15(a)). This evidence is not surprising, as [40,41] have demonstrated, using potential flow analysis, how for blades with negligible thickness the absolute exit angle α_2 is only a function of blade solidity. This result has been experimentally observed also in [42] for a variable speed Wells turbine. Fig. 15(a) highlights that the value of α_2

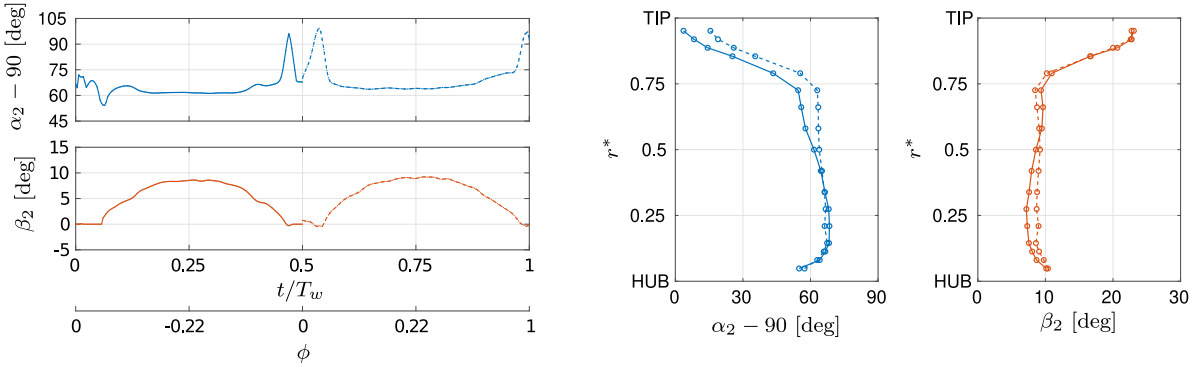

(a) Flow angles at blade midspan. (b) Flow angles for $\phi = 0.22$.

Fig. 15. Outlet flow angles distributions during the inflow (solid line) and outflow phase (dashed line).

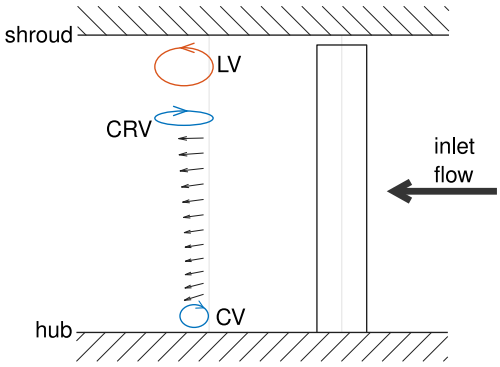

Fig. 16. Schematic view of the likely secondary flow structures downstream of the Wells rotor, in the meridian plane.

is almost constant during the two phases, except near the inversions. Only small differences can be observed between the two phases along the blade span, Fig. 15(b), although more discrepancies are detected in the tip region where a strong radial gradient can be observed due to the presence of a leakage flow. More interestingly, Fig. 15(b) clearly highlights the effects associated to the leakage flow and to the rotor solidity at the blade root, which determine a decrease in the absolute flow angle in both regions due to the lower work exchanged. The larger variation near the tip is due to the combined presence of high axial velocities due to the leakage flow. The smaller absolute angles in the hub and tip regions result in larger relative angles in the same regions. The secondary flow structures suggested by the flow distribution shown in Fig. 14 are schematically presented in Fig. 16: the leakage vortex LV caused by the leakage flow, a contra-rotating vortex induced by the LV, the corner vortex CV at the hub, and the main flow drawn towards the hub region because of the particular work distribution.

4.4. Local performance analysis

Based on the flow measurements during the inflow phase, when the inlet velocity component is completely axial, it is interesting to evaluate the blade design law of the tested Wells turbine. Traditional Wells turbine rotors are built maintaining the blade chord constant along the span, but to the authors' knowledge no considerations on the design law have been ever reported. Referring to the inflow phase, i.e. $C_{1,\theta} \approx 0$, the blade general whirl distribution can be defined as follows:

$$\frac{C_{2,\theta}}{U_{tip}} = A + B(r^*)^n \tag{11}$$

where the coefficients A, B and n have been evaluated between 20 and 75% of the blade span, where wall proximity effects are not present, as shown in Fig. 17(a), using a least-square fitting.

The evaluated design law provides a value of the exponent of about 2 ($n = 1.98$) while A and B are equal to -0.397 and 0.209, respectively, with 95% confidence bounds. The design law is represented in Fig. 17(a) with a dashed curve, and has been used to estimate the non-dimensional Euler work, represented in Fig. 17(b) again with dashed curve, and shown together with the corresponding values evaluated from the velocity components, with a very good agreement outside the boundary layer regions. This representation gives an important indication of wall proximity effects on the actual work, which is strongly reduced in the hub and tip regions. In particular, the reduction in blade load in the tip region is clearly highlighted in Fig. 17(b), resulting in almost 20% of the blade affected by reduced performance. It should also be observed that the design law results in a reduction of the work exchanged at larger radii, which is in agreement with the variation in blade solidity. This suggests that Wells rotors designed with constant solidity along the blade span would be able to exchange higher work at larger radii. This hypothesis, that is supported also by numerical results on global performance in [43], requires more detailed investigations on the local flow field, both with experiments and numerical simulations. In fact, the flow in the tip region is influenced by intense secondary flows which result in non-linear three-dimensional effects [43] that modify the expected distributions.

Turbine local performance is reported in Fig. 18 considering the parameters defined in Eqs. (7) and (8), as a function of non-dimensional blade radius and piston period. These representations show that the specific work locally exchanged, Fig. 18(a), is almost equal during the inflow and outflow phases, except in the tip region where only a slight increase in the outflow phase is present, mainly associated to the higher values of $C_{2,\theta}$ detected in this region. The effect of the lower incidence angle, see Figs. 12(e) and 13, is, in fact, compensated by the higher relative velocity of the flow, with the two opposite effects balancing for this specific geometry. Despite this result, the total-to-static efficiency during the inflow phase is moderately higher, as shown in Fig. 18(b), coherently to what observed for the global efficiency in Fig. 10(b): up to 5% difference can be appreciated with respect to the outflow phase.

Fig. 19 presents a comparison of the tangentially averaged radial distributions of non-dimensional work and total-to-static efficiency, during inflow and outflow, for two values of the flow coefficient (0.15 and 0.22). This comparison confirms what qualitatively presented in the maps of Fig. 18, showing minor differences between inflow and outflow for the specific work, mainly in the tip region and for the lower operating condition. The local total-to-static efficiency is lower in the outflow phase than during inflow at both operating conditions. This is associated to the different exhaust kinetic energy, larger during the outflow phase, while the contribution of the rotor losses does not to vary between the two phases, as confirmed by an almost equal distribution of the specific work ψ (Fig. 18(a)).

The maps of Fig. 20 show the loss contributions ξ_R and ξ_{EX} as a function of non-dimensional blade radius and piston period. Loss

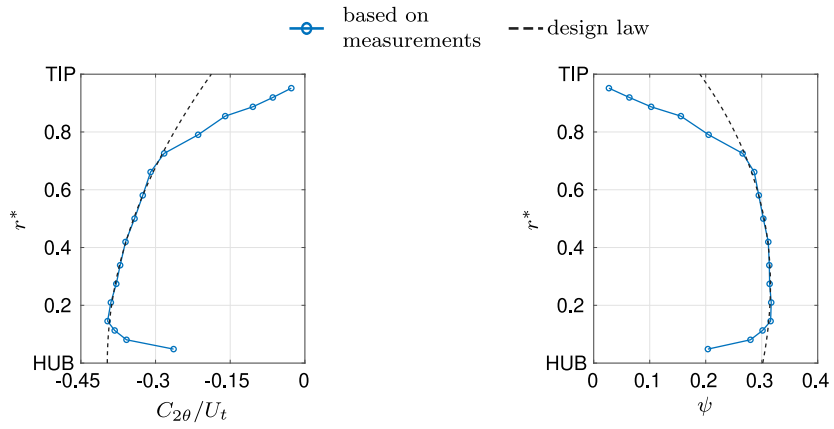

(a) Outlet tangential velocity. (b) Work coefficient.

Fig. 17. Blade design law at $\phi = 0.22$ for the inflow phase.

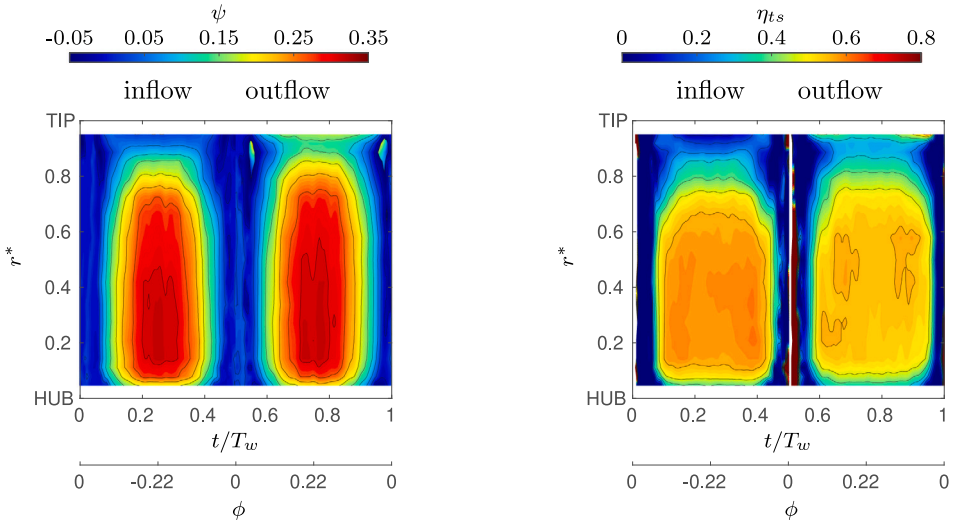

(a) Work coefficient. (b) Total-to-static efficiency.

Fig. 18. Maps of the turbine performance parameters for a complete piston period.

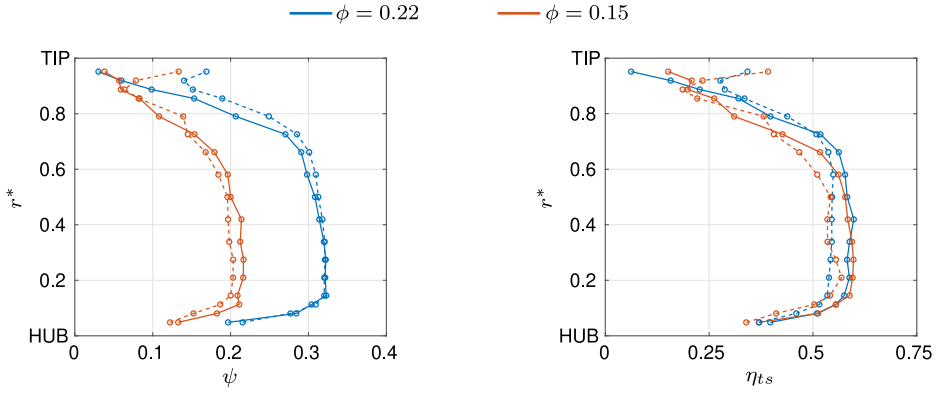

(a) Work coefficient. (b) Efficiency.

Fig. 19. Radial distribution of performance for inflow (solid line) and outflow phases (dashed line), for two different flow conditions.

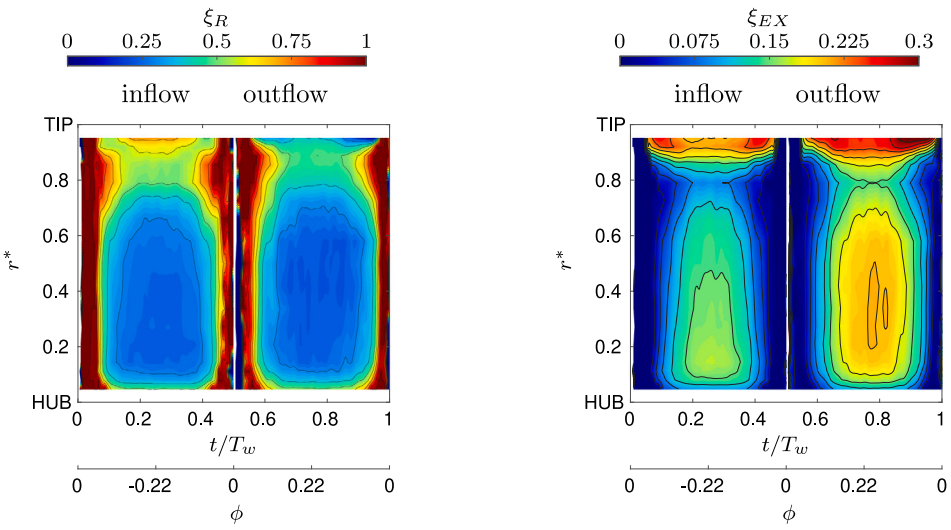

(a) Rotor losses. (b) Exit losses.

Fig. 20. Maps of the non-dimensional loss contributions for a complete piston period.

contribution maps confirm what expected from considerations based on ψ and η_{ts} results. In fact, the rotor losses ξ_R show similar values between inflow and outflow phases, with the exception of a small variation near the tip, due to a variation of $C_{2,\theta}$ for the same $C_{2,z}$ and $C_{2,r}$, as shown in Fig. 14(a-c). These differences in the outlet tangential velocity component can be reasonably related to the different inlet flow during inflow and outflow phases, due to the swirl component at the rotor inlet observed during the outflow phase. On the other hand, exit kinetic energy losses show remarkable differences between the two phases, with always larger values at every radial position during the outflow phase. This depends on the higher values of the exhaust kinetic energy, well shown in Fig. 14(c), and results in a moderately lower total-to-static efficiency in the outflow phase.

5. Conclusions

This work presents an extensive experimental investigation of the three-dimensional flow field upstream and downstream of the rotor of a monoplane Wells turbine. The unsteady tests, conducted in an OWC simulator under regular wave motion, have been carried out measuring both overall and local flow quantities. For the latter, a 4-holes aerodynamic pressure probe specifically designed for these investigations has been employed. The main findings of this detailed investigation can be summarized as follows.

- The presence of a residual swirl flow inside the chamber modifies the inlet flow during the outflow phase, resulting in a lower incidence angle at every radial position and a simultaneous increase in relative velocity.
- This inlet flow distortion results in a slightly higher value of the maximum output torque and in a delayed stall in the outflow phase. A lower value of the aerodynamic efficiency is therefore calculated for the same flow coefficient during outflow.
- The lower total-to-static efficiency during the outflow phase is due to the larger exit kinetic energy losses observed at every radial position, while rotor losses show only minor differences in the tip region.
- The flow can reasonably be considered bi-dimensional in a wide portion of the blade span, while wall proximity effects at the tip and the hub result in a strongly three-dimensional flow behavior in these regions.
- In particular, the tip region is affected by the presence of the leakage flow, which extends for about 20% of the blade span, interacting with the clean flow and reducing the local performance (work exchanged and efficiency).
- The higher solidity at the blade root exerts a blockage on the inlet flow, resulting in a three-dimensional exit flow which is compatible with the presence of a corner vortex confined in the hub region.
- The blade design law obtained keeping the chord length constant along the blade radius corresponds to a parabolic design law which is intrinsically responsible for a reduction of the work exchanged in the tip region.
- A moderate negative radial component of velocity is present at the outlet. Its origin can be ascribed to the design law of the blade (lower work exchanged at higher radial positions).

This work provides important insights for the local flow field inside a Wells turbine coupled to an OWC simulator. It can be an useful set of data to search for geometric modifications aimed at improving Wells rotor performance, and it provides a good basis for a detailed validation of numerical tools.

Funding

This study was carried out within the "e.INS - Ecosystem of Innovation for Next Generation Sardinia" funded by the Italian Ministry of University and Research under the Next-Generation EU Programme (National Recovery and Resilience Plan - PNRR, M4C2, INVESTMENT 1.5 - DD 1056 of 23/06/2022, ECS00000038). This manuscript reflects only the authors' views and opinions, neither the European Union nor the European Commission can be considered responsible for them.

CRediT authorship contribution statement

Fabio Licheri: Writing – review & editing, Writing – original draft, Visualization, Investigation, Formal analysis, Data curation. **Tiziano Ghisu:** Writing – review & editing, Visualization, Supervision, Formal analysis, Data curation. **Francesco Cambuli:** Writing – review & editing, Supervision, Project administration, Funding acquisition. **Pierpaolo Puddu:** Writing – review & editing, Writing – original draft, Visualization, Methodology, Data curation, Conceptualization.

Declaration of competing interest

The authors declare the following financial interests/personal relationships which may be considered as potential competing interests: Fabio Licheri reports financial support was provided by Italian Ministry of University and Research - e.INS project. Francesco Cambuli reports financial support was provided by Italian Ministry of University and Research - e.INS project.

Data availability

Data will be made available on request.

References

[1] Gunn K, Stock-Williams C. Quantifying the global wave power resource. Renew Energy 2012;44:296–304. http://dx.doi.org/10.1016/j.renene.2012.01.101.

[2] Arinaga RA, Cheung KF. Atlas of global wave energy from 10 years of reanalysis and hindcast data. Renew Energy 2012;39(1):49–64. http://dx.doi.org/10.1016/j.renene.2011.06.039.

[3] Guo C, Sheng W, De Silva DG, Aggidis G. A review of the levelized cost of wave energy based on a Techno-Economic model. Energies 2023;16(5). http://dx.doi.org/10.3390/en16052144.

[4] Curto D, Franzitta V, Guercio A. Sea wave energy. A review of the current technologies and perspectives. Energies 2021;14(20). http://dx.doi.org/10.3390/en14206604.

[5] Wells A. Fluid driven rotary transducer - BR. Pat. 1595700. 1976.

[6] Raghunathan S, Tan C, Wells N. Theory and performance of a Wells turbine. J Energy 1982;6(2):157–60. http://dx.doi.org/10.2514/3.48047.

[7] Gato LMC, Falcão AFdO. On the theory of the Wells turbine. J Eng Gas Turbines Power 1984;106(3):628–33. http://dx.doi.org/10.1115/1.3239616.

[8] Gato L, de O. Falcão A. Aerodynamics of the Wells turbine. Int J Mech Sci 1988;30(6):383–95. http://dx.doi.org/10.1016/0020-7403(88)90012-4.

[9] Starzmann R, Moisel C, Carolus T, Tease K, Arlitt R. Assessment method of sound radiated by cyclically operating Wells turbines. Int J Mar Energy 2013;2:12–27. http://dx.doi.org/10.1016/j.ijome.2013.05.004.

[10] Stefanizzi M, Camporeale SM, Torresi M. Experimental investigation of a Wells turbine under dynamic stall conditions for wave energy conversion. Renew Energy 2023;214:369–82. http://dx.doi.org/10.1016/j.renene.2023.05.120.

[11] Kumar A, Das TK, Samad A. Experimental study of Wells turbine with multiparameter modification for wave energy conversion. In: OCEANS 2021: San Diego – Porto. 2021, p. 1–7. http://dx.doi.org/10.23919/OCEANS44145.2021.9705898.

[12] Puddu P, Paderi M, Manca C. Aerodynamic characterization of a Wells turbine under bi-directional airflow. In: Energy procedia, 68th conference of the Italian thermal machines engineering association, ATI2013, vol. 45, 2014, p. 278–87. http://dx.doi.org/10.1016/j.egypro.2014.01.030.

[13] Setoguchi T, Takao M, Kaneko K. Hysteresis on Wells turbine characteristics in reciprocating flow. Int J Rotating Mach 1998;4(1):17–24. http://dx.doi.org/10.1155/S1023621X98000025.

[14] Raghunathan S, Ombaka O. Effect of frequency of air flow on the performance of the Wells turbine. Int J Heat Fluid Flow 1985;6(2):127–32. http://dx.doi.org/10.1016/0142-727X(85)90049-9.

[15] Takao M, Setoguchi T, Nagata S, Toyota K. A study on the effects of blade profile and non-uniform tip clearance of the Wells turbine. In: International conference on offshore mechanics and arctic engineering, Volume 6: Nick Newman Symposium on Marine Hydrodynamics; Yoshida and Maeda Special Symposium on Ocean Space Utilization; Special Symposium on Offshore Renewable Energy, 2008, p. 625–32. http://dx.doi.org/10.1115/OMAE2008-57235.

[16] Das TK, Kumar K, Samad A. Experimental analysis of a biplane Wells turbine under different load conditions. Energy 2020;206:118205. http://dx.doi.org/10.1016/j.energy.2020.118205.

[17] Das TK, Samad A. Influence of stall fences on the performance of Wells turbine. Energy 2020;194:116864. http://dx.doi.org/10.1016/j.energy.2019.116864.

[18] Watterson J, Raghunathan S. Investigation of Wells turbine performance using 3-D CFD. In: IECEC 96. proceedings of the 31st intersociety energy conversion engineering conference. vol. 3, 1996, p. 1777–82. http://dx.doi.org/10.1109/IECEC.1996.553371, vol.3.

[19] Torresi M, Camporeale S, Strippoli P, Pascazio G. Accurate numerical simulation of a high solidity Wells turbine. Renew Energy 2008;33(4):735–47. http://dx.doi.org/10.1016/j.renene.2007.04.006.

[20] Nazeryan M, Lakzian E. Detailed entropy generation analysis of a Wells turbine using the variation of the blade thickness. Energy 2018;143:385–405. http://dx.doi.org/10.1016/j.energy.2017.11.006.

[21] Licheri F, Cambuli F, Puddu P, Ghisu T. A comparison of different approaches to estimate the efficiency of Wells turbines. J Fluids Eng 2021;143(5). http://dx.doi.org/10.1115/1.4049686.

[22] Alves JS, Gato LM, Falcão AF, Henriques JC. Experimental investigation on performance improvement by mid-plane guide-vanes in a biplane-rotor Wells turbine for wave energy conversion. Renew Sustain Energy Rev 2021;150:111497. http://dx.doi.org/10.1016/j.rser.2021.111497.

[23] Morais F, Carrelhas A, Gato L. Biplane-rotor Wells turbine: The influence of solidity, presence of guide vanes and comparison with other configurations. Energy 2023;276:127514. http://dx.doi.org/10.1016/j.energy.2023.127514.

[24] Licheri F, Puddu P, Ghisu T, Cambuli F. Experimental analysis of the unsteady flow inside a Wells turbine. 2021;312:11009. http://dx.doi.org/10.1051/e3sconf/202131211009.

[25] Paderi M, Puddu P. Experimental investigation in a Wells turbine under bi-directional flow. Renew Energy 2013;57:570–6. http://dx.doi.org/10.1016/j.renene.2013.02.016.

[26] Licheri F, Ghisu T, Cambuli F, Puddu P. Experimental analysis of the three-dimensional flow in a Wells turbine rotor. Int J Turbomach, Propuls Power 2023;8(3). http://dx.doi.org/10.3390/ijtpp8030021.

[27] Curran R, Gato LMC. The energy conversion performance of several types of Wells turbine designs. Proc Inst Mech Eng A 1997;211(2):133–45. http://dx.doi.org/10.1243/0957650971537051.

[28] Gato LMC, Webster M. An experimental investigation into the effect of rotor blade sweep on the performance of the variable-pitch Wells turbine. Proc Inst Mech Eng A 2001;215(5):611–22. http://dx.doi.org/10.1243/0957650011538848.

[29] Licheri F, Ghisu T, Cambuli F, Puddu P. Detailed investigation of the local flow-field in a Wells turbine coupled to an OWC simulator. Renew Energy 2022;197:583–93. http://dx.doi.org/10.1016/j.renene.2022.07.116.

[30] Shehata AS, Xiao Q, Saqr KM, Alexander D. Wells turbine for wave energy conversion: a review. Int J Energy Res 2017;41(1):6–38. http://dx.doi.org/10.1002/er.3583.

[31] Dhanasekaran T, Govardhan M. Computational analysis of performance and flow investigation on Wells turbine for wave energy conversion. Renew Energy 2005;30(14):2129–47. http://dx.doi.org/10.1016/j.renene.2005.02.005.

[32] Bryer DW, Pankhurst RC. Pressure-probe methods for determining wind speed and direction. Aeronaut J 1971;75(729):126. http://dx.doi.org/10.1017/S0001924000046315.

[33] Cherrett M, Bryce J, Hodson H. The 3D pneumatic and 2D dynamic probes: Their development and subsequent use in a transonic fan. Defence Research Agency Farnborough (UK); 1992, p. 18, Technical Memo, ADA262559.

[34] Notaristefano A, Gaetani P, Dossena V, Fusetti A. Uncertainty evaluation on multi-hole aerodynamic pressure probes. J Turbomach 2021;143(9):091001. http://dx.doi.org/10.1115/1.4050452.

[35] Coleman HW, Glenn Steel Jr W. Experimentation, validation, and uncertainty analysis for engineers. 3rd ed.. John Wiley & Sons, Ltd; 2009, http://dx.doi.org/10.1002/9780470485682.fmatter.

[36] Ghisu T, Cambuli F, Puddu P, Virdis I, Carta M, Licheri F. A lumped parameter model to explain the cause of the hysteresis in OWC-Wells turbine systems for wave energy conversion. Appl Ocean Res 2020;94. http://dx.doi.org/10.1016/j.apor.2019.101994.

[37] Raghunathan S, Tan CP, Ombaka OO. Performance of the Wells self-rectifying air turbine. Aeronaut J 1985;89:369–79. http://dx.doi.org/10.1017/S0001924000096743.

[38] Ghisu T, Cambuli F, Puddu P, Virdis I, Carta M, Licheri F. A critical examination of the hysteresis in Wells turbines using computational fluid dynamics and lumped parameter models. J Offshore Mech Arct Eng 2020;142(5). http://dx.doi.org/10.1115/1.4046379.

[39] Schlichting H, Gersten K. Boundary-layer theory. 9th ed.. Springer Berlin, Heidelberg; 2016, http://dx.doi.org/10.1007/978-3-662-52919-5.

[40] Falcão AFO, Gato LMC. 8.05 - Air turbines. In: Comprehensive renewable energy. Oxford: Elsevier; 2012, p. 111–49. http://dx.doi.org/10.1016/B978-0-08-087872-0.00805-2.

[41] Raghunathan S. The Wells air turbine for wave energy conversion. Prog Aerosp Sci 1995;31(4):335–86. http://dx.doi.org/10.1016/0376-0421(95)00001-F.

[42] Licheri F, Puddu P, Cambuli F, Ghisu T. Experimental investigation on a speed controlled wells turbine for wave energy conversion. In: International conference on offshore mechanics and arctic engineering, Volume 8: Ocean Renewable Energy, 2022, V008T09A077. http://dx.doi.org/10.1115/OMAE2022-80986.

[43] Torresi M, Pranzo D, Camporeale S, Pascazio G. Improved design of high solidity Wells turbine. In: Proceedings of the 9th European wave and tidal energy conference. Southampton, UK; 2011.